

High quality-factor terahertz phonon-polaritons in layered lead iodide

Received: 26 September 2025

Accepted: 23 January 2026

Cristiane N. Santos, Flávio H. Feres, Théo Hannotte, Romain Peretti, Mathias Vanwolleghem, Sophie Eliet, Benjamin Walter, Marc Faucher, Adrian Cernescu, Raul O. Freitas & Jean-François Lampin

Cite this article as: Santos, C.N., Feres, F.H., Hannotte, T. *et al.* High quality-factor terahertz phonon-polaritons in layered lead iodide. *Nat Commun* (2026). <https://doi.org/10.1038/s41467-026-69027-6>

We are providing an unedited version of this manuscript to give early access to its findings. Before final publication, the manuscript will undergo further editing. Please note there may be errors present which affect the content, and all legal disclaimers apply.

If this paper is publishing under a Transparent Peer Review model then Peer Review reports will publish with the final article.

High quality-factor terahertz phonon-polaritons in layered lead iodide

Cristiane N. Santos^{1*}, Flávio H. Feres², Théo Hannotte¹, Romain Peretti^{1,3}, Mathias Vanwolleghem¹, Sophie Eliet¹, Benjamin Walter⁴, Marc Faucher^{1,4}, Adrian Cernescu⁵, Raul O. Freitas^{2*}, Jean-François Lampin^{1*}

¹Institute of Electronics, Microelectronics and Nanotechnology (IEMN), Université de Lille, UMR CNRS 8520, Avenue Poincaré, Villeneuve d'Ascq, 59652, France.

²Brazilian Synchrotron Light Laboratory (LNLS), Brazilian Center for Research in Energy and Materials (CNPEM), 13083-100, Campinas, Brazil.

³CNRS, National Institute of Applied Sciences of Lyon (INSA Lyon), Ecole Centrale de Lyon (ECL), Université Claude Bernard Lyon 1, CPE Lyon, INL, UMR CNRS 5270, Villeurbanne, 69100, France.

⁴Vmicro SAS, 27 rue Charles Saint Venant, Hellennes, 59260, France.

⁵attocube systems GmbH, Eglfinger Weg 2, Haar, 85540, Germany.

*Corresponding author(s). E-mail(s): nsantos.cristiane@gmail.com; raul.freitas@lnls.br; jean-francois.lampin@univ-lille.fr;

Abstract

While hyperbolic phonon-polaritons in van der Waals materials such as h-BN and α -MoO₃ have driven major advances in mid-infrared (IR) nanophotonics, further progress at longer THz wavelengths has been hampered due to material limitations and experimental challenges. Here, we report the discovery of long-lived hyperbolic phonon-polaritons in the deep THz range in layered PbI₂. Using room-temperature scattering-type scanning near-field optical microscopy, we achieved real-space imaging and broadband spectral analysis of PbI₂ 2D crystals transferred onto different substrates with high near-field amplitude contrast and good agreement with theoretical models. Our measurements revealed an experimental figure-of-merit related to the propagating efficiency of the polaritons above

15—on par with state-of-the-art mid-IR benchmarks—and extreme field confinement of 264 for a 144 nm-thick flake, which can exceed 300 in slightly thinner samples. These findings demonstrate that PbI_2 combines strong anisotropy, low losses, and extreme mode confinement, making it a compelling candidate for deep-THz nanophotonic applications.

Keywords: terahertz nanophotonics, s-SNOM, hyperbolic phonon polaritons, 2D lead iodide, van der Waals materials

Introduction

Just over a decade ago, the experimental demonstration of low-loss propagating hyperbolic phonon-polaritons (HPhPs) in hexagonal boron nitride (h-BN)^[1] marked the beginning of a new era in infrared (IR) nanophotonics and sub-diffractive waveguiding^[2]. Phonon-polaritons—well known as light propagation modes strongly coupled to atomic vibrations—occur in polar dielectrics and signal intense interaction between light and lattice dynamics. In specific frequency ranges where this coupling is strongest, light is almost entirely reflected by the dielectric, forming the so-called Reststrahlen bands (RBs). When extended to two-dimensional (2D) materials, these RBs became highly valuable for nanophotonics due to their pronounced anisotropy, originating from strong in-plane covalent bonds and weak out-of-plane van der Waals (vdW) interlayer interactions. This anisotropy can be so pronounced that the dielectric permittivity tensors in 2D vdW crystals exhibit opposite signs along directions parallel and perpendicular to the stacked layers. As a result, a unique dispersion relation emerges, where the isofrequency surface becomes a hyperboloid^[3, 4], giving rise to the HPhP designation. Within this framework, HPhP dispersion can be passively tuned by adjusting the number of monolayers^[1] or by modifying the interlayer spacing through intercalation^[5]. This tunability is enabled by the fact that light propagates within the volume of the 2D crystals, making HPhPs a crucial element for light transport in future nanophotonic circuits.

These discoveries in h-BN nanophotonics sparked a surge of interest in identifying new nanomaterials capable of supporting HPhPs. Notable examples include h-BN^[1], $\alpha\text{-V}_2\text{O}_5$ ^[5], $\alpha\text{-MoO}_3$ ^[6, 7], Bi_2Se_3 ^[8, 9], SnO_2 ^[10], TeO_2 ^[11], GeS ^[12], HfS_2 and HfSe_2 ^[13]—all members of the vdW family with active HPhP modes spanning from IR to far-IR. These materials now lead a revolutionary front in nanotechnology, where HPhP energy flow can be precisely tailored. Canalized light in $\alpha\text{-MoO}_3$ ^[14–17] and $\alpha\text{-V}_2\text{O}_5$ ^[18] twisted bilayers, topological modulation of polaritons dispersion in h-BN metasurfaces^[19], lower-symmetry shear HPhPs^[20] and naturally canalized light in LiV_2O_5 ^[21] are all examples of engineered 2D systems expanding the functional landscape for HPhP-based mid-to-far IR applications. However, this revolution has not yet reached deep THz frequencies (e.g. 0.3 to 3 THz) and as a result, none of the IR nanophotonics advances described above are currently being explored for long-wavelength HPhPs. This gap can be attributed to both the limited knowledge of 2D

materials capable of supporting HPhPs with high quality factors and the experimental challenges associated with operating nanoscale analytical techniques in the THz range.

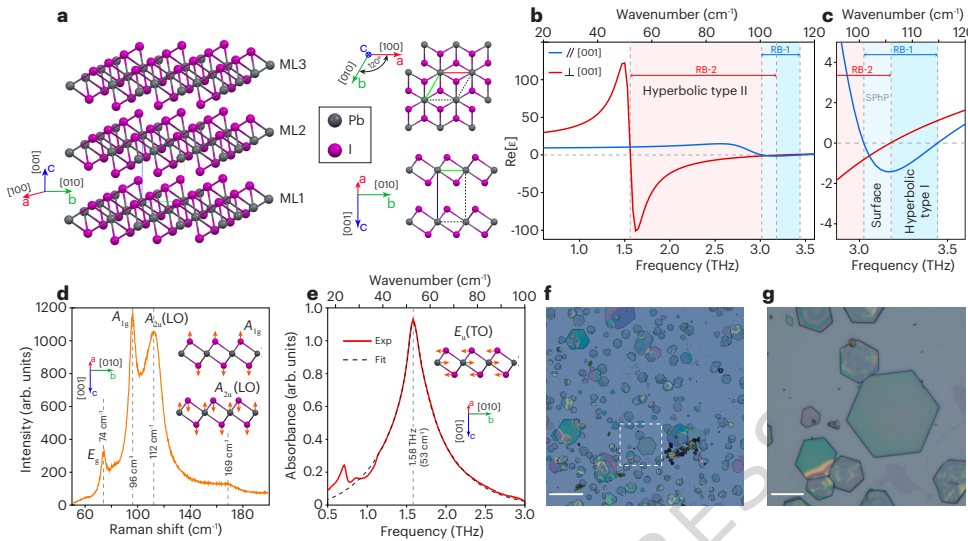


Fig. 1 PbI₂ crystal structure, vibrational response and dielectric properties in the THz range. **a**, Monolayer (ML) arrangement of the atomic lattices of PbI₂ with top and side views of its unit cell. **b**, Overview of its real part of the permittivity and delimitation of hyperbolic, surface and Reststrahlen bands. Ranges for the Reststrahlen bands type 1 (RB-1) and type 2 (RB-2) are indicated. **c**, Detailed view of the permittivity in the range between 95-120 cm⁻¹ comprising hyperbolic and surface phonon-polaritons (SPhP). **d**, Raman spectrum of PbI₂ flakes with indication of the active modes. **e**, Far-field THz Time-Domain Spectroscopy (TDS) absorption spectrum of an isolated PbI₂ crystal fitted by a phenomenological model (Supplementary Information, Section 7). **f**, Optical microscopy image of the PbI₂ crystals transferred to a Si substrate. **g**, Zoomed optical image with fine details of the 2D crystals (area within the white dashed square in f). Scale bars in f,g represent 50 μ m and 10 μ m, respectively.

Here, we introduce lead iodide (PbI₂) as a model 2D material that supports extremely confined HPhPs in the deep THz range, with propagation efficiency comparable to benchmark 2Ds in the IR range. We used scattering Scanning Near-field Optical Microscopy (s-SNOM)[22–25], an ultra-microscopy technique capable of probing the nano-optical properties of materials [26, 27], to obtain real-space THz imaging and spectral analysis of 2D PbI₂ flakes with excellent amplitude contrast and precise agreement with theory.

Results and Discussion

PbI₂ is a vdW semiconductor with a direct bandgap of 2.34 eV atomically organized as a layered CdI₂-type structure (space group P $\bar{3}$ m1, Fig. 1a). It is also known as the rare mineral Bustamentite, and its most common stacking forms are 2H and 4H. The

4H polymorph typically forms in samples grown from the melt, via precipitation, or through sublimation, whereas the 2H polymorph is generally produced via hydrothermal or sol-gel synthesis. In our case, crystalline PbI_2 hexagonal micro-platelets (Fig. 1f,g) were synthesized via hydrothermal process (Methods, Supplementary Information, Section 5), a simple and accessible method for producing high-quality 2D PbI_2 crystals. Compared with h-BN, PbI_2 exhibits negligible isotopic variability, enabling sustainable large-scale crystal growth and ensuring reproducibility in future device applications. While standard hBN is typically composed of approximately 20% ^{10}B and 80% ^{11}B , resulting in significant mass variation between standard and isotopically purified hBN, iodide is monoisotopic, and lead consists of only three naturally occurring isotopes, predominantly ^{207}Pb with minimal variation. Consequently, PbI_2 exhibits a natural mass fluctuation of less than $\pm 0.5\%$, a critical factor for achieving high phonon Q-factors and ensuring devices future reproducibility. Due to its composition of heavy elements, PbI_2 has been proposed as a material for X-ray and gamma-ray detectors[28, 29] and more recently as precursor in the fabrication of highly efficient perovskite solar cell materials, including $\text{CH}_3\text{NH}_3\text{PbI}_3$, $\text{CH}(\text{NH}_2)_2\text{PbI}_3$, and CsPbI_3 . Generally an excess of PbI_2 is present in these materials as protrusions [30, 31] and can serve as a passivation layer[32, 33]. The optical properties of PbI_2 , including Raman scattering and far-infrared behavior, were first investigated in the 1960-1970s and in subsequent studies[34–38]. On its optical phonon modes, two are Raman-active (E_g and A_{1g}), and two are infrared-active (A_{2u} and E_u). The E_u mode corresponds to an in-plane vibration (Fig. 1e), excited when the electric field lies within the plane (perpendicular to the crystal c-axis, Fig. 1e inset). We experimentally revisited the Raman spectrum of the 2D PbI_2 as shown in Fig. 1d. Besides the expected Raman-active modes E_g and A_{1g} , we observed the infrared-active A_{2u} mode, whose presence is detectable due to its coupling with the A_{1g} mode [39, 40]. These modes correspond to vibrations perpendicular to the plane (parallel to the c-axis, see Fig. 1d inset). The $A_{2u}(\text{TO})$ mode was earlier studied by FTIR reflection measurements [41]. Additionally, we characterized the $E_u(\text{TO})$ mode applying far-field time-domain THz spectroscopy (TDS) on a large PbI_2 crystal in transmission geometry (Supplementary Material, Section 7) and confirmed a strong absorption band centered at 1.58 THz (53 cm^{-1}), as shown in Fig. 1e. As shown in Fig. 1b,c, a strong anisotropy is observed between the phonon frequencies of 1.55 THz ($\nu_{E_u}(\text{TO})$) and 2.85 THz ($\nu_{A_{2u}}(\text{TO})$). As a result, PbI_2 behaves as a hyperbolic material of type II in the frequency range of 1.55–3.03 THz ($52\text{--}101 \text{ cm}^{-1}$, Fig. 1b) and of type I between 3.24–3.45 THz ($108\text{--}115 \text{ cm}^{-1}$, Fig. 1c). A surface phonon-polariton (SPhP) band is observed in the overlapping region between RB-1 and RB-2, where the real part of the permittivity tensor components are both negative (Fig. 1c). Notably, the hyperbolic band type II in PbI_2 is rather broad pointing to a very large dielectric anisotropy. As a consequence, PbI_2 exhibits enhanced ionicity, a property linked to the Born Effective Charge (BEC) and therefore associated with the degree of electron transfer in chemical bonds and polarization response to atomic displacements[42]. This particular frequency dependence of the PbI_2 permittivity tensor arises from the combination of strong anisotropy and a very broad RB associated with its ionic character. Further in this work, we qualitatively assess ionicity using the Lyddane–Sachs–Teller (LST) relation $\varepsilon_0/\varepsilon_\infty = \omega_{LO}^2/\omega_{TO}^2$ [43].

From the pioneering studies by A. Grisel *et al.*[36] and G. Lucovsky *et al.*[37] in the 1970s, it was evident that the extreme anisotropy in the permittivity of PbI_2 would give rise to an ultra-wide RB in the THz range. Figures 1b,c show the real part of the in-plane (red solid lines) and out-of-plane (blue solid lines) permittivity, calculated using the optical constants reported in [37, 38] (see Supplementary Information, Section 3). These studies also established that its CdI_2 -type structure is organized as a lamellar layered material held together by vdW forces. Despite its properties being known for decades, this material is only now being introduced as a promising 2D medium for sub-diffractive THz nanophotonics unveiled by s-SNOM. Figure 2a presents a representative illustration of our THz s-SNOM setup (Methods and Supplementary Information, Section 6) used for real-space imaging of HPhPs in PbI_2 2D crystals. A ~ 20 mW THz beam (2.52 THz, 84 cm^{-1}), generated by a CO_2 -pumped methanol laser, illuminates a long-shaft (70 μm) Pt-coated Si AFM tip (Supplementary Information, Section 8), enabling field confinement at length scales comparable to the tip radius (~ 40 nm)[44, 45]. The tip-scattered THz signal is detected by a Schottky diode in a homodyne scheme, with background suppression achieved via established [25] higher-harmonics demodulation. The top-right inset of Fig. 2a shows an experimental near-field image of a 655 nm-thick PbI_2 crystal, revealing an amplitude ripple pattern that was further modeled (bottom-right inset of Fig. 2a) using a multiple-sources model based on Hertzian dipole antennas (HDA, Supplementary Information, Section 3.3) [46], supporting the polaritonic nature of the waves.

The origin of the near-field amplitude patterns is further investigated through Fourier transform (FT) analysis of the s-SNOM images. Figure 2b shows intensity profiles extracted from the FT of the near-field amplitude image of the 655 nm-thick flake (inset of Fig. 2b). The FT profiles, taken along the three directions indicated by the dashed lines in the q -space map in the inset of Fig. 2b, exhibit strong peaks at $\pm 2.48 \times 10^4 \text{ cm}^{-1}$, indicating a dominant wavelength of 2.53 μm in the analyzed wave pattern. Both real-space and Fourier analyses of these waves (Fig. 2b,d) reveal a periodicity that precisely matches the predicted λ_p of phonon-polaritons in the RB-2 region of PbI_2 , thereby confirming PbI_2 as a 2D platform for HPhPs. Figure 2c displays near-field amplitude images of PbI_2 flakes with various thicknesses, showing a clear variation in the spacing between intensity fringes as a function of thickness. These s-SNOM images reveal pronounced amplitude contrast with a signal-to-noise ratio (SNR) sufficient to resolve at least three oscillation maxima for all investigated thicknesses. All s-SNOM amplitude images presented in Fig. 2c were median leveled and then normalized by an average value of the substrate response. The reproducibility of the waves across all examined crystals indicates a consistent and well-defined crystallinity in the 2D PbI_2 produced in this work. These amplitude oscillations are further analyzed in Fig. 2d, where near-field amplitude profiles extracted across the edge of the PbI_2 flakes highlight a clear relationship between the crystal thickness and fringe wavelength. To validate the hypothesis of polaritonic activity, we calculated a dispersion diagram for various PbI_2 thicknesses within the frequency range of its RB-2, as shown in Fig. 2e. A horizontal dashed line indicates the illumination frequency of 2.52 THz, enabling estimation of the q -value for the measured samples. From the dispersion diagram in Fig. 2e, a continuous estimate for $\lambda_p = 2\pi/q$ for thicknesses

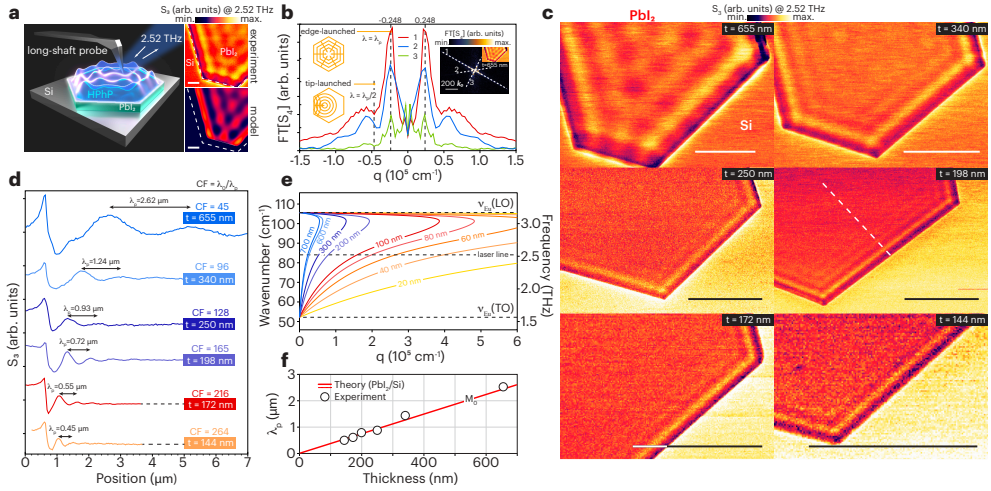


Fig. 2 Real-space nano-imaging of THz hyperbolic phonon-polaritons (HPhPs) in PbI_2 . **a**, Graphical illustration of the THz scattering scanning near-field optical microscopy (s-SNOM) scheme accessing HPhPs activity with a long metallic atomic force microscopy (AFM) tip, upper right: near-field amplitude image of a 655 nm-thick flake at 2.52 THz, lower right: corresponding calculated HPhP waves pattern (see Supplementary Information, Section 3.2). Scale bars in the insets represent 2 μm . **b**, Fourier transform (FT) profiles of the near-field image of the 655 nm-thick flake highlighting sharp peaks centered at q -values inversely proportional to the HPhPs wavelength. Inset: Fourier transform image with indication (white dashed lines) of the directions from where the profiles were extracted (see Supplementary Information, Section 2.2). **c**, Near-field images of flakes with various thicknesses (t) measured at 2.52 THz. Scale bars in c represent 5 μm . **d**, Near-field amplitude profiles extracted from the nanoscopy images (dashed white line in c) displaying the HPhP wavelength variation with the flake thickness. The confinement factor ($\text{CF} = \lambda_0/\lambda_p$) is presented for each thickness. λ_0 and λ_p represent the excitation and polariton wavelengths, respectively. **e**, Frequency-momentum (ω - q) dispersion relation of HPhPs between the transverse optical phonon frequency $\nu_{E\text{u}}(\text{TO}) = 1.55$ THz and the longitudinal phonon frequency $\nu_{E\text{u}}(\text{LO}) = 3.18$ THz calculated for various thicknesses (Supplementary Information, Section 3.1). **f**, HPhP wavelength (λ_p) estimated from the FT analysis versus crystal thickness (open circles: experimental data, red line: calculation from the dispersion diagram).

ranging from 0 to 700 nm is presented in Fig. 2f (red curve), where experimental λ_p (open circles), extracted from the FFT analysis (Supplementary Information, Section 2.2), show excellent agreement. This confirms that the observed wavelengths correspond to the HPhP wavelength λ_p , therefore, we determine that the HPhP launching mechanism is predominantly driven by the PbI_2 edges in that case.

As previously established in the mid-IR range and extensively studied in h-BN [1, 47–50], the underlying assumption is that two mechanisms govern the launching of HPhPs: (i) polariton waves are launched by a metallic tip and reflected back from the crystal edges (round-trip between tip and edge), where the oscillation period corresponds to half of the polariton wavelength, $\lambda_p/2$ (inset in Fig. 2b, bottom left); (ii) HPhPs are launched by the edge propagating as plane waves reaching the tip, where the interference of near-fields from the HPhPs and illuminated tip are re-scattered into the far-field, forming a standing wave pattern parallel to the crystal edge with a

periodicity of λ_p (inset in Fig. 2b, top left). In h-BN and other hyperbolic materials in the mid-IR range, the tip typically serves as the primary launcher of polaritons. However, its superior efficiency as a launcher is not always evident, as both mechanisms are often observed within the same measurement. Additionally, tip-launched HPhPs undergo geometric decay and require a round-trip from the edge to be re-coupled to the tip [47], increasing the challenge for their observation. A comprehensive FT analysis of the entire set of flakes is presented in the Supplementary Information Section 2.2, where small contribution of $\lambda_p/2$ is observed when the crystal is analyzed on a dielectric substrate. One important aspect to consider is that our experiments operated with wavelengths nearly an order of magnitude longer than those typically used in the mid-IR, thereby increasing the illumination spot size and, therefore, increasing the interaction cross-section with the sample. This becomes evident in the real-space THz images of the PbI_2 flakes, which display a homogeneous scattering response along all edges of the flakes (see Fig. 2c). Moreover, our hydrothermal synthesis method reliably produces crystals with geometries that precisely follow the PbI_2 unit cell arrangement, where the edges of the 2D crystals taper to form sharp facets. This is confirmed by scanning electron microscopy, as detailed in the Supplementary Information Section 1. In this configuration, the edges act as efficient HPhP launchers under far-field illumination but, on the other hand, serve as low-efficiency reflectors for internal HPhP waves, making the observation of tip-launched round-trip polaritons more challenging.

To further explore the nanophotonics of PbI_2 , we employed THz near-field time-domain spectroscopy (nano-TDS) to access the full extent of its RB-2. Our experimental setup was based on integrating a fiber-based TDS system into a s-SNOM nanoscope, as illustrated in Fig. 3a. As a s-SNOM-based technique, nano-TDS enables access to the optical properties of materials in a typical range of 0.5 to 3 THz in point-spectroscopy mode.

Figure 3b presents the nano-TDS point-spectrum acquired at the center of a 298 nm-thick PbI_2 crystal deposited onto Si. The near-field amplitude and phase are consistent with the expected THz reflectivity and absorption of PbI_2 within this range, showing excellent agreement with the far-field TDS measurements (Fig. 1e). To assess the HPhP behavior in the material, we performed a spatial-spectral analysis as shown in Fig. 3c. Along a line crossing the edge of the 298 nm-thick PbI_2 crystal (Fig. 3c inset), multiple near-field amplitude point-spectra were collected, revealing contrast between the Si substrate and the 2D flake. On the PbI_2 crystal—starting at its edge (position 0 μm)—the point-spectra exhibit two intensity maxima that consistently shift to lower frequencies as the probe moves away from the edge, in agreement with the dispersive nature of PbI_2 HPhPs within the RB-2 region. Conversely, at fixed frequencies, the spacing between the two fringes increases, *i.e.*, λ_p becomes longer at lower excitation frequencies. This trend is precisely captured in Fig. 3d, where experimental amplitude profiles at selected frequencies (open circles) are extracted from the spatial-spectral map (white arrows in Fig. 3c indicate the analyzed frequencies). We employed a phenomenological model that considers the tip and edge as distinct polariton launchers with different geometric decays (Supplementary Information, Section 3.4) to fit the experimental data (red curve) and extract key HPhP wave parameters, such as amplitude, wavelength, and damping [4–6, 51]. The same model was used to

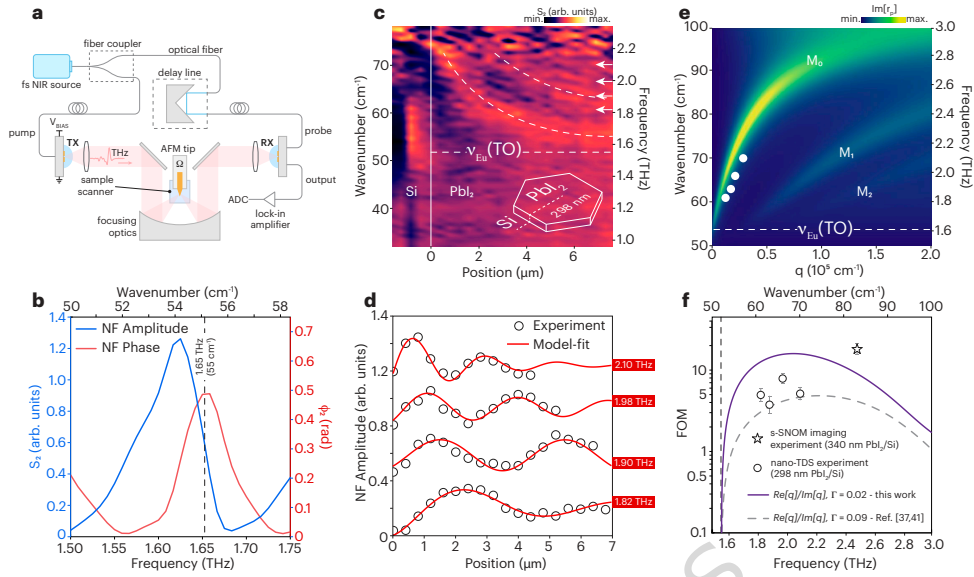


Fig. 3 THz nano-TDS analysis. **a**, Schematic of the THz s-SNOM TDS experimental setup that employs a fs near-infrared (NIR) source to pump a transmitter (TX) and a receiver (RX) whose signal is digitized by an analog-to-digital converter (ADC). **b**, Near-field complex spectra (2nd harmonic) measured at the center of a PbI₂ flake featuring an absorption peak consistent to the E_u (TO) mode. **c**, s-SNOM TDS spectral-linescan across the PbI₂ edge (see inset scheme) displaying spatial-spectral amplitude modulations for a 298 nm-thick flake. Two amplitude maxima are recorded as the tip moves away from the edge (position 0 μm), showing a dispersive trend. White dashed lines guide the eyes for the visualization of the amplitude dispersion and the ν_{E_u} (TO) frequency. **d**, Amplitude profiles extracted from c at four different frequencies and fitted to a parameters-retrieval model (Supplementary Information, Section 3.4). **e**, Dispersion diagram of the HPhPs (color map: imaginary part of the Fresnel reflection coefficient r_p , white dots: experimental points). **f**, PbI₂ HPhPs figure-of-merit (FOM) versus frequency (solid and dashed lines: theoretical FOM; circles and star: extracted from experimental data). Experimental uncertainty bars were calculated via standard error propagation in the fitting procedure described in the Supplementary Information, Section 3.4. Γ is the damping parameter that represents the dielectric losses in the dielectric function (see Supplementary Information, Eq. S4).

extract the HPhP parameters from the real-space images at 2.52 THz shown in Figure 2c, by fitting the profiles presented in Figure 2d (Supplementary Information, Section 3.4). Figure 3e shows an overlay of these experimentally derived data points (white dots) onto the theoretical ω - q dispersion of the imaginary part of the Fresnel reflectivity (r_p) for the 298 nm-thick PbI₂ crystal. The data closely follow the dispersion of the first-order branch (M_0) of PbI₂ HPhPs, demonstrating good agreement between experiment and theory. These parameters are further used to estimate an experimental figure-of-merit (FOM) related to the propagation efficiency of the observed waves. In line with common practice in this research field $\frac{\text{Re}[q]}{\text{Im}[q]}$ has been chosen as an indicator of the quality of the observed phonon polariton. This allows to compare our results with previous HPhP observations well established in mid-infrared frequencies.

However, care should be taken not to confuse this figure-of-merit with the true quality factor of the guided HPhPs, $Q = \omega\tau$ with τ the photon lifetime. This latter can only be correctly evaluated by also taking into account the group velocity of the guided HPhP, as $\tau = 1/(\text{Im}[q]v_g)$. Figure 3f presents FOM values obtained from the nano-TDS (open circles) and s-SNOM narrowband imaging (open star) experiments. These experimental FOM values were compared with theoretical predictions (calculated as the ratio $\text{Re}[q]/\text{Im}[q]$ for $t=298$ nm), showing reasonable agreement. Upon closer inspection, this theoretical estimate of the FOM exhibits a strong dependence on the dielectric losses of PbI_2 , represented by the damping parameter (Γ) used in the dielectric function. The dashed curve in Figure 3f shows the FOM calculated using $\Gamma = 0.09$, a value adopted from G. Lucovsky *et al.* [37, 41] experimentally extracted from far-field THz reflectance measurements in the 1970s. In contrast, the theoretical estimate based on our near-field results (solid curve in Fig. 3f) indicates substantially lower dielectric losses, with $\Gamma = 0.02$ yielding an average FOM curve that aligns well with our data from both broadband TDS and narrowband s-SNOM experiments.

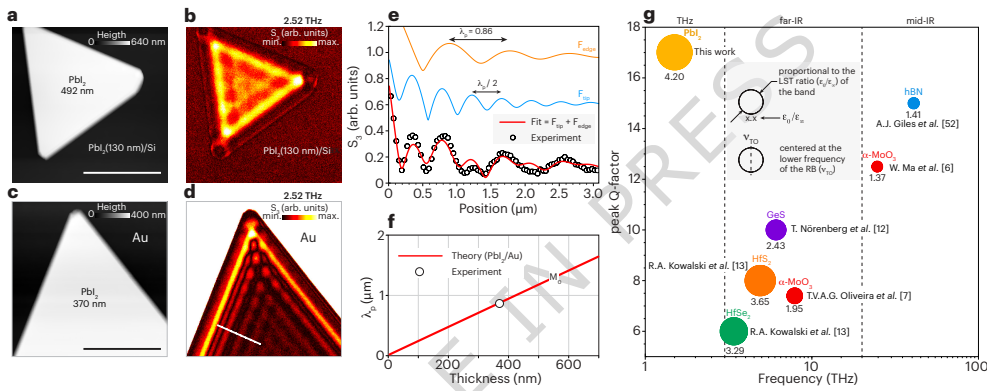


Fig. 4 PbI_2 as an HPhP cavity on different substrates and in comparison to other phonon-polaritonic media. **a,b**, AFM and near-field amplitude images of a 492 nm-thick PbI_2 crystal on a 130 nm-thick PbI_2 crystal on Si measured at 2.52 THz. The near-field image reveals a high-contrast standing wave pattern of HPhPs within the triangular crystal. Scale bar: 10 μm . **c,d**, AFM and s-SNOM amplitude images of a 370 nm-thick triangular PbI_2 flake on Au, highlighting an interference pattern formed by HPhP waves launched by both the tip and crystal edges. Scale bar: 5 μm . **e**, Experimental near-field amplitude profile (open circles) extracted along the white dashed line in panel d, fitted by a phenomenological function (red line) that accounts for HPhPs launched by the edge (orange line) and the tip (blue line). **f**, Expected polariton wavelengths as a function of PbI_2 thickness when transferred onto an Au substrate for 2.52 THz illumination. The experimental data point (open circle) is obtained from the analysis in panel e (Supplementary Information, Section 3.3). **g**, PbI_2 in the context of other selected 2D materials supporting HPhPs across the mid-IR, far-IR, and THz ranges, organized by their key parameters FOM and Lyddane–Sachs–Teller (LST) relation. ν_{TO} represents the frequency of the transverse optical (TO) phonon mode. ϵ_0 and ϵ_∞ represent PbI_2 dielectric constants at the low and high frequency limits, respectively.

In Fig. 4, we present an evaluation of PbI_2 functioning as an HPhP standing-wave cavity on both dielectric and metallic substrates. Figures 4a,b show the topography of

a 492 nm-thick triangular crystal grown on a 130 nm-thick PbI_2 crystal on Si and the corresponding near-field amplitude image acquired at 2.52 THz. The third-harmonic near-field amplitude image (Fig. 4b) reveals high-contrast HPhP interference patterns within the crystal. Similar strong contrast is observed for HPhP waves in a 370 nm-thick PbI_2 crystal on Au, where one corner of a triangular flake was analyzed (Figs. 4c,d). A double periodicity is evident in the near-field image of Fig. 4d, from which an amplitude profile (white dashed line) was extracted and fitted using the model described previously (Supplementary Information, Section 3.4). In this case, the function accounts for both tip-launched (F_{tip}) and edge-launched (F_{edge}) polaritons, as shown in Fig. 4e. From this fitting, we estimated the polariton wavelength λ_p for the analyzed PbI_2/Au system, which matches well with the theoretical prediction presented in Fig. 4f. The use of a metallic substrate enhances the tip-induced dipole, thereby increasing the SNR and strengthening the coupling between the tip and the PbI_2 flake. Consequently, the double-periodicity interference pattern observed confirms the coexistence of both edge- and tip-launched HPhP waves in the experiment conducted on Au substrate (Fig. 4d). Furthermore, Figs. 4b,d reveal outstanding propagation efficiency of the HPhP waves for both Si and Au substrates, demonstrating the versatility of the material for use as a THz resonator or in the development of microscale THz cavities. Finally, we position PbI_2 among other prominent hyperbolic 2D materials by comparing key properties, including the FOM $\text{Re}[q]/\text{Im}[q]$ and the LST ratio, as shown in Fig. 4g. Notably, only PbI_2 (THz, FOM = 17), for a 340 nm-thick crystal (Fig. 2c), and h-BN (mid-IR, FOM = 15 [52]) exhibit values exceeding 15. Other emerging hyperbolic materials in the far-IR range—including GeS [12], α - MoO_3 [6, 7], HfSe_2 and HfS_2 [13]—display lower FOM values, with α - MoO_3 reaching a maximum of 12.4 in the mid-IR. Figure 4g also reports the LST ratio for each material, with magnitude values indicated below each data point and marker size scaled proportionally for visual comparison. The very high dielectric anisotropy and large ionicity of PbI_2 are key advantages, enabling its hyperbolic response across an ultra-wide spectral range. This property is qualitatively assessed by calculating the LST ratio for the type II hyperbolic band of PbI_2 , which is then compared to other prominent materials in this class. The LST ratio reaches 4.20 for PbI_2 , while for h-BN (RB-2) and HfSe_2 (RB-2) [13], this ratio is 1.41 and 3.29, respectively.

This work introduces a hyperbolic material with compelling nanophotonic activity across an ultra-wide band in the deep terahertz range. Our s-SNOM experimental data exhibit enhanced SNR, enabling high contrast in real-space visualization of THz phonon-polaritons, with excellent agreement with established theory. We measured HPhPs with FOM values reaching 17, positioning PbI_2 as a competitive platform alongside h-BN and α - MoO_3 , now extended into the THz regime. The field confinement also surpasses that of most materials in this class, with a measured λ_0/λ_p of 264 for a 144 nm-thick PbI_2 . This confinement factor can exceed 300 for flakes thinner than 100 nm under the same illumination (2.52 THz). In the production perspective, 2D PbI_2 is facile to synthesize, composed of relatively abundant elements, and exhibits chemical stability under standard ambient conditions. Compared to mechanical exfoliation, its common growth methods offer scalability and potential for practical

integration. As a semiconductor, it also supports carrier injection—whether electrical, optical, or via doping—enabling coupling to phonons and paving the way for active components like modulators and detectors. As a vdW material, PbI_2 can also be stacked with other 2D materials [53–55], further expanding its range of potential applications. In conclusion, PbI_2 emerges as a compelling platform for THz nanophotonics, offering both fundamental advantages and a pathway toward practical device integration. Its ability to support long-wavelength hyperbolic phonon polaritons, with inherently lower momentum requirements, eases many of the coupling challenges that currently limit higher-order polaritonic modes in the mid-IR regime [56, 57]. This property positions PbI_2 as a candidate for enabling compact on-chip light-routing elements and advanced wave manipulation concepts. Moreover, the recent introduction of multifunctional 2D materials such as PdSe_2 for IR detection [58] highlights the technological momentum of polaritonic circuitry, which can be naturally extended into the THz domain with PbI_2 . Altogether, PbI_2 provides a versatile material foundation for enabling polariton-mediated phenomena and driving the development of next-generation THz optoelectronic and nanophotonic devices.

Methods

PbI_2 crystals synthesis

Crystals were grown using a simple hydrothermal technique and deposited on a high-resistivity silicon wafer for the Raman and s-SNOM experiments, except for the experiment in Fig. 4c-d that we used Au(100 nm)/Si as a substrate. Larger flakes were grown in a solution following the same technique and transferred above a hole drilled in a metallic foil for transmission THz TDS (see Supplementary Information Section 5 for details).

Far-field pre-characterization

Raman spectroscopy measurements on PbI_2 flakes (Fig. 1d) were performed using a micro-photoluminescence and Raman setup based on a LabRAM HR confocal system (Horiba Jobin-Yvon). For Raman experiments, we employed a 633 nm laser source for excitation. The scattered light was analyzed using an 800 mm focal length monochromator, with detection provided by a CCD camera covering the 0.3 to 1.06 μm spectral range. We used a notch filter to reject Rayleigh scattered light below 50 cm^{-1} . Far-field THz transmission spectra (Fig. 1e) were acquired using a commercial time-domain spectroscopy (TDS) system (TeraSmart, Menlo Systems GmbH), which employs a pulsed THz source based on a photoconductive antenna excited by a femtosecond laser, along with a synchronously gated photoconductive detector. An oscillating delay line was used to reconstruct the temporal profile of the electric field. A large PbI_2 flake ($\sim 4 \mu\text{m}$ -thick) was mounted over a 500 μm pinhole in a 100 μm -thick metallic plate. The THz beam was focused and collected using TPX lenses with a 38 mm diameter and 50 mm focal length. All measurements were performed under a dry nitrogen atmosphere to minimize water vapor absorption. The spectra were obtained by averaging 1000 scans (120 ps-long) with a 33 fs time step and subsequently normalized to

a reference measurement taken through an identical empty pinhole. Further details on the setup and measurement procedure are provided in the Supplementary Information Section 7.

THz s-SNOM imaging

s-SNOM images (Figures 2c and 4a-d) were acquired using a commercial near-field nanoscope (NeaSNOM, attocube systems GmbH) illuminated by a continuous-wave (CW) terahertz source based on a CO₂ laser-pumped molecular laser (FIRL100, Edinburgh Instruments Ltd.). The THz cavity was filled with low-pressure methanol (CH₃OH) vapor, with the CO₂ laser tuned to the 9P36 line to generate lasing at 2522.78 GHz. Under optimal pressure conditions, the typical THz output power, measured using a thermopile, was approximately 70 mW. The beam was directed toward the s-SNOM system, where a 12 μ m-thick Mylar beamsplitter divided it into two paths: a reference arm and the tip-sample interaction stage. Parabolic optics focused the THz radiation onto a metallic AFM probe, which acts as an antenna to confine a portion of the incident field at its apex, enabling nanoscale THz imaging. We estimated \sim 20 mW to reach the tip-sample stage. For the s-SNOM images shown in Fig. 2c, we used 70 μ m-long Pt-coated Si probes (Vmicro SAS, 270 kHz) with an apex radius of approximately 40 nm (Supplementary Information, Section 8), operating with tapping amplitudes around 100 nm and an integration time of 20 ms per pixel. For the images in Fig. 4a-d, we used 80 μ m-long full-metal probes (80 kHz, 25PtIr200B-H40, Rocky Mountain Nanotechnology LLC) with tapping amplitudes of approximately 120 nm and a pixel integration time of 10 ms. All s-SNOM measurements were performed using a homodyne scheme (reference mirror fixed in an optimized position to maximize the near-field signal). Background suppression was achieved by demodulating the signal at the third harmonic of the cantilever's resonance frequency. Signal detection was performed using a room-temperature Schottky diode detector/mixer (WM86, Virginia Diodes Inc.).

THz s-SNOM nanospectroscopy

THz nano-TDS experiments were done using a commercial instrument (THz-neaSCOPE⁺S, attocube systems GmbH) equipped with an integrated THz time-domain spectroscopy module (TeraSmart, Menlo Systems GmbH). THz pulses covering the spectral range 0.5-2.5 THz are generated and coherently detected by a photoconductive pair of antennas. A conductive AFM tip with a shaft length of 80 μ m and typical average tip radius of \sim 40 nm (25PtIr200B-H40, Rocky Mountain Nanotechnology LLC), operated in non-contact tapping mode (at a nominal frequency of 80 kHz), acts as a nanofocusing probe, allowing for simultaneous capture of sample topography together with measurements of the scattered near-field signal in a single scan of the sample. Experimental data presented in Fig. 3b,c were acquired in a nitrogen purged environment with relative humidity below 5% to minimize the presence of water-vapor absorption lines in the detected THz spectra. Background subtraction was done via higher harmonic demodulation at the second harmonic of the tip tapping frequency. Point-spectrum in Fig. 3b was acquired in the middle of a 298 nm-thick PbI₂ flake

where only the dielectric response was detected by the tip (no back-reflected polariton waves from the edges at this position). The spectrum was averaged from 10 interferograms. Spectra-linescan in Fig. 3c was measured across the the edge of the same flake, where 25 point-spectra were acquired along the 10 μm -long dashed line indicated in the Fig. 3c inset. For each point-spectrum, we averaged 5 interferograms. For all nano-TDS experiments the probe amplitude was kept at 150 nm, pixel time was set as 50 ms and spectral resolution was 0.03 THz (30 ps scanning delay). All spectra were normalized by a reference spectrum taken on Au/Si substrate.

Data availability. Relevant data supporting the key findings of this study are available within the article and the Supplementary Information file. All raw data generated during the current study are available from the corresponding authors upon request.

References

- [1] Dai, S., Fei, Z., Ma, Q., Rodin, A.S., Wagner, M., McLeod, A.S., Liu, M.K., Gannett, W., Regan, W., Watanabe, K., Taniguchi, T., Thiemens, M., Dominguez, G., Neto, A.H.C., Zettl, A., Keilmann, F., Jarillo-Herrero, P., Fogler, M.M., Basov, D.N.: Tunable Phonon Polaritons in Atomically Thin van der Waals Crystals of Boron Nitride. *Science* **343**(6175), 1125–1129 (2014) <https://doi.org/10.1126/science.1246833>
- [2] Caldwell, J.D., Aharonovich, I., Cassabois, G., Edgar, J.H., Gil, B., Basov, D.N.: Photonics with hexagonal boron nitride. *Nature Reviews Materials* **4**(8), 552–567 (2019) <https://doi.org/10.1038/s41578-019-0124-1>
- [3] Basov, D.N., Fogler, M.M., Abajo, F.J.G.: Polaritons in van der Waals materials. *Science* **354**(6309), 1992 (2016) <https://doi.org/10.1126/science.aag1992>
- [4] Low, T., Chaves, A., Caldwell, J.D., Kumar, A., Fang, N.X., Avouris, P., Heinz, T.F., Guinea, F., Martin-Moreno, L., Koppens, F.: Polaritons in layered two-dimensional materials. *Nature Materials* **16**(2), 182–194 (2017) <https://doi.org/10.1038/nmat4792>
- [5] Taboada-Gutiérrez, J., Álvarez-Pérez, G., Duan, J., Ma, W., Crowley, K., Prieto, A. Iván and Bylinkin, Autore, M., Volkova, H., Kimura, K., Kimura, T., Berger, M.-H., Li, S., Bao, Q., Gao, X.P.A., Errea, I., Nikitin, A.Y., Hillenbrand, J. Rainerand Martín-Sánchez, Alonso-González, P.: Broad spectral tuning of ultra-low-loss polaritons in a van der Waals crystal by intercalation. *Nature Materials* **19**, 964–968 (2020) <https://doi.org/10.1038/s41563-020-0665-0>
- [6] Ma, W., Alonso-González, P., Li, S., Nikitin, A.Y., Yuan, J., Martín-Sánchez, J., Taboada-Gutiérrez, J., Amenabar, I., Li, P., Vélez, S., Tollar, C., Dai, Z., Zhang, Y., Sriram, S., Kalantar-Zadeh, K., Lee, S.-T., Hillenbrand, R., Bao, Q.: In-plane anisotropic and ultra-low-loss polaritons in a natural van der Waals crystal. *Nature* **562**, 557–562 (2018) <https://doi.org/10.1038/s41586-018-0618-9>

[7] Oliveira, T.V.A.G., Nörenberg, T., Álvarez-Pérez, G., Wehmeier, L., Taboada-Gutiérrez, J., Obst, M., Hempel, F., Lee, E.J.H., Klopf, J.M., Errea, I., Nikitin, A.Y., Kehr, S.C., Alonso-González, P., Eng, L.M.: Nanoscale-confined terahertz polaritons in a van der Waals crystal. *Advanced Materials* **33**(2), 2005777 (2021) <https://doi.org/10.1002/adma.202005777>

[8] Pogna, E.A.A., Viti, L., Politano, A., Brambilla, M., Scamarcio, G., Vitiello, M.S.: Mapping propagation of collective modes in Bi₂Se₃ and Bi₂Te_{2.2}Se_{0.8} topological insulators by near-field terahertz nanoscopy. *Nature Communications* **12**(1), 1–11 (2021) <https://doi.org/10.1038/s41467-021-26831-6>

[9] Chen, S., Bylinkin, A., Wang, Z., Schnell, M., Chandan, G., Li, P., Nikitin, A.Y., Law, S., Hillenbrand, R.: Real-space nanoimaging of THz polaritons in the topological insulator Bi₂Se₃. *Nature Communications* **13**(1), 1374 (2022) <https://doi.org/10.1038/s41467-022-28791-x>

[10] Feres, F.H., Mayer, R.A., Wehmeier, L., Maia, F.C.B., Viana, E.R., Malachias, A., Bechtel, H.A., Klopf, J.M., Eng, L.M., Kehr, S.C., González, J.C., Freitas, R.O., Barcelos, I.D.: Sub-diffractive cavity modes of terahertz hyperbolic phonon polaritons in tin oxide. *Nature Communications* **12**(1), 1995 (2021) <https://doi.org/10.1038/s41467-021-22209-w>

[11] Mayer, R.A., Wehmeier, L., Torquato, M., Chen, X., Feres, F.H., Maia, F.C.B., Obst, M., Kaps, F.G., Luferau, A., Klopf, J.M., Gilbert Corder, S.N., Bechtel, H.A., González, J.C., Viana, E.R., Eng, L.M., Kehr, S.C., Freitas, R.O., Barcelos, I.D.: Paratellurite Nanowires as a Versatile Material for THz Phonon Polaritons. *ACS Photonics* (2024) <https://doi.org/10.1021/acsphotonics.4c01249>

[12] Nörenberg, T., Álvarez-Pérez, G., Obst, M., Wehmeier, L., Hempel, F., Klopf, J.M., Nikitin, A.Y., Kehr, S.C., Eng, L.M., Alonso-González, P., Oliveira, T.V.A.G.: Germanium monosulfide as a natural platform for highly anisotropic thz polaritons. *ACS Nano* **16**(12), 20174–20185 (2022) <https://doi.org/10.1021/acsnano.2c05376>

[13] Kowalski, R.A., Mueller, N.S., Álvarez-Pérez, G., Obst, M., Diaz-Granados, K., Carini, G., Senarath, A., Dixit, S., Niemann, R., Iyer, R.B., Kaps, F.G., Wetzel, J., Klopf, J.M., Kravchenko, I.I., Wolf, M., Folland, T.G., Eng, L.M., Kehr, S.C., Alonso-Gonzalez, P., Paarmann, A., Caldwell, J.D.: Ultraconfined terahertz phonon polaritons in hafnium dichalcogenides. *Nature Materials* **24**(11), 1735–1741 (2025) <https://doi.org/10.1038/s41563-025-02345-0>

[14] Hu, G., Ou, Q., Si, G., Wu, Y., Wu, J., Dai, Z., Krasnok, A., Mazor, Y., Zhang, Q., Bao, Q., Qiu, C.W., Alù, A.: Topological polaritons and photonic magic angles in twisted α -MoO₃ bilayers. *Nature* **582**(7811), 209–213 (2020) <https://doi.org/10.1038/s41586-020-2359-9>

[15] Duan, J., Capote-Robayna, N., Taboada-Gutiérrez, J., Álvarez-Pérez, G., Prieto,

I., Martín-Sánchez, J., Nikitin, A.Y., Alonso-González, P.: Twisted Nano-Optics: Manipulating Light at the Nanoscale with Twisted Phonon Polaritonic Slabs. *Nano Letters* **20**(7), 5323–5329 (2020) <https://doi.org/10.1021/acs.nanolett.0c01673>

[16] Chen, M., Lin, X., Dinh, T.H., Zheng, Z., Shen, J., Ma, Q., Chen, H., Jarillo-Herrero, P., Dai, S.: Configurable phonon polaritons in twisted α -MoO₃. *Nature Materials* **19**(12), 1307–1311 (2020) <https://doi.org/10.1038/s41563-020-0732-6>

[17] Duan, J., Álvarez-Pérez, G., Lanza, C., Voronin, K., Tresguerres-Mata, A.I.F., Capote-Robayna, N., Álvarez-Cuervo, J., Tarazaga Martín-Luengo, A., Martín-Sánchez, J., Volkov, V.S., Nikitin, A.Y., Alonso-González, P.: Multiple and spectrally robust photonic magic angles in reconfigurable α -MoO₃(3) trilayers. *Nature materials* **22**(7), 867–872 (2023) <https://doi.org/10.1038/s41563-023-01582-5>

[18] Shiravi, H., Zheng, W., He, Y., Ran, S., Rhodes, D.A., Balicas, L., Zhou, H.D., Ni, G.X.: Twist-engineered phonon polaritons in α -V₂O₅. *Opt. Lett.* **50**(9), 2986–2989 (2025) <https://doi.org/10.1364/OL.557267>

[19] Li, P., Dolado, I., Alfaro-Mozaz, F.J., Casanova, F., Hueso, L.E., Liu, S., Edgar, J.H., Nikitin, A.Y., Vélez, S., Hillenbrand, R.: Infrared hyperbolic metasurface based on nanostructured van der Waals materials. *Science* **359**(6378), 892–896 (2018) <https://doi.org/10.1126/science.aaq1704>

[20] Passler, N.C., Ni, X., Hu, G., Matson, J.R., Carini, G., Wolf, M., Schubert, M., Alù, A., Caldwell, J.D., Folland, T.G., Paarmann, A.: Hyperbolic shear polaritons in low-symmetry crystals. *Nature* **602**(7898), 595–600 (2022) <https://doi.org/10.1038/s41586-021-04328-y>

[21] F. Tresguerres-Mata, A.I., Lanza, C., Taboada-Gutiérrez, J., Matson, J.R., Álvarez-Pérez, G., Isobe, M., Tarazaga Martín-Luengo, A., Duan, J., Partel, S., Vélez, M., Martín-Sánchez, J., Nikitin, A.Y., Caldwell, J.D., Alonso-González, P.: Observation of naturally canalized phonon polaritons in LiV₂O₅ thin layers. *Nature Communications* **15**(1), 2696 (2024) <https://doi.org/10.1038/s41467-024-46935-z>

[22] Zenhausern, F., Martin, Y., Wickramasinghe, H.K.: Scanning interferometric apertureless microscopy: optical imaging at 10 angstrom resolution. *Science (New York, N.Y.)* **269**(5227), 1083–5 (1995) <https://doi.org/10.1126/science.269.5227.1083>

[23] Kawata, S., Inouye, Y.: Scanning probe optical microscopy using a metallic probe tip. *Ultramicroscopy* **57**(2-3), 313–317 (1995) [https://doi.org/10.1016/0304-3991\(94\)00159-K](https://doi.org/10.1016/0304-3991(94)00159-K)

[24] Knoll, B., Keilmann, F.: Near-field probing of vibrational absorption for chemical microscopy. *Nature* **399**(6732), 134–137 (1999) <https://doi.org/10.1038/20154>

- [25] Keilmann, F., Hillenbrand, R.: Near-field microscopy by elastic light scattering from a tip. *Philosophical transactions. Series A, Mathematical, physical, and engineering sciences* **362**(1817), 787–805 (2004) <https://doi.org/10.1098/rsta.2003.1347>
- [26] Chen, X., Hu, D., Mescall, R., You, G., Basov, D.N., Dai, Q., Liu, M.: Modern Scattering-Type Scanning Near-Field Optical Microscopy for Advanced Material Research. *Advanced Materials* **31**(24), 1–24 (2019) <https://doi.org/10.1002/adma.201804774>
- [27] Hillenbrand, R., Abate, Y., Liu, M., Chen, X., Basov, D.N.: Visible-to-THz near-field nanoscopy. *Nature Reviews Materials* **10**(4), 285–310 (2025) <https://doi.org/10.1038/s41578-024-00761-3>
- [28] Shah, K.S., Street, R.A., Dmitriev, Y., Bennett, P., Cirignano, L., Klugerman, M., Squillante, M.R., Entine, G.: X-ray imaging with pbi2-based a-sih flat panel detectors. *Nuclear Instruments and Methods in Physics Research Section A: Accelerators, Spectrometers, Detectors and Associated Equipment* **458**(1), 140–147 (2001) [https://doi.org/10.1016/S0168-9002\(00\)00857-3](https://doi.org/10.1016/S0168-9002(00)00857-3)
- [29] Shah, K.S., Bennett, P., Klugerman, M., Moy, L., Cirignano, L., Dmitriev, Y., Squillante, M.R., Olschner, F., Moses, W.W.: Lead iodide optical detectors for gamma ray spectroscopy. *IEEE Transactions on Nuclear Science* **44**(3), 448–450 (1997) <https://doi.org/10.1109/23.603688>
- [30] Zizlsperger, M., Nerreter, S., Yuan, Q., Lohmann, K.B., Sandner, F., Schiegl, F., Meineke, C., Gerasimenko, Y.A., Herz, L.M., Siday, T., Huber, M.A., Johnston, M.B., Huber, R.: In situ nanoscopy of single-grain nanomorphology and ultrafast carrier dynamics in metal halide perovskites. *Nature Photonics* **18**(9), 975–981 (2024) <https://doi.org/10.1038/s41566-024-01476-1>
- [31] Hieulle, J., Krishna, A., Boziki, A., Audinot, J.-N., Farooq, M.U., Machado, J.F., Mladenović, M., Phirke, H., Singh, A., Wirtz, T., Tkatchenko, A., Graetzel, M., Hagfeldt, A., Redinger, A.: Understanding and decoupling the role of wavelength and defects in light-induced degradation of metal-halide perovskites. *Energy Environmental Science* **17**, 284–295 (2024) <https://doi.org/10.1039/D3EE03511E>
- [32] Chen, Y., Meng, Q., Xiao, Y., Zhang, X., Sun, J., Han, C.B., Gao, H., Zhang, Y., Lu, Y., Yan, H.: Mechanism of PbI_2 in situ passivated perovskite films for enhancing the performance of perovskite solar cells. *ACS Applied Materials & Interfaces* **11**(47), 44101–44108 (2019) <https://doi.org/10.1021/acsami.9b13648>
- [33] Rothmann, M.U., Kim, J.S., Borchert, J., Lohmann, K.B., O’Leary, C.M., Shearer, A.A., Clark, L., Snaith, H.J., Johnston, M.B., Nellist, P.D., Herz, L.M.: Atomic-scale microstructure of metal halide perovskite. *Science* **370**(6516), 5940 (2020) <https://doi.org/10.1126/science.abb5940>

<https://www.science.org/doi/pdf/10.1126/science.abb5940>

- [34] Mon, J.-P.: Spectres de vibrations de quelques cristaux d'iodures métalliques à structure lamellaire. *Comptes Rendus* **262B**, 493–495 (1966)
- [35] Carabatos, C.: Etude expérimentale et théorique de la diffusion raman de CdI₂ et PbI₂. *Comptes Rendus* **272B**, 465–468 (1971)
- [36] Grisel, A., Schmid, P.: Polytypism and lattice vibrations of PbI₂. *Phys. Stat. Sol. b* **73**, 587–591 (1976)
- [37] Lucovsky, G., White, R.M., Liang, W.Y., Zallen, R., Schmid, P.: The lattice polarizability of PbI₂. *Solid State Commun.* **18**, 811–814 (1976)
- [38] Chang, Y.-C., James, R.B.: Phonon dispersion and polar-optical scattering in 2H PbI₂. *Physical Review B* **55**, 8219–8225 (1997)
- [39] Nakashima, S.: Raman study of polytypism in vapor-grown PbI₂. *Solid State Communications* **16**(9), 1059–1062 (1975) [https://doi.org/10.1016/0038-1098\(75\)90003-4](https://doi.org/10.1016/0038-1098(75)90003-4)
- [40] Khilji, M.Y., Sherman, W.F., Wilkinson, G.R.: Raman study of three polytypes of PbI₂. *Journal of Raman Spectroscopy* **13**(2), 127–133 (1982) <https://doi.org/10.1002/jrs.1250130206>
- [41] Lucovsky, G., White, R.M.: Optical-Phonon Anisotropies in Layered Crystals. II *Nuovo Cimento* **38**(1), 290–300 (1977) <https://doi.org/10.1007/BF02723498>
- [42] Pauling, L.: *The Nature of Chemical Bond*, 1st edn. Cornell University Press, Cornell University Press (1960)
- [43] Ashcroft, N.W., Mermin, D.: *Solid State Physics*, 1st edn. Brooks Cole, Pacific Grove (1976)
- [44] Walter, B., Mairiaux, E., Vignaud, D., Eliet, S., Lampin, J.-F., Faucher, M.: Terahertz near-field imaging using batch-fabricated cantilevers with 70 μ m long tips. Paper presented at the 44th International Conference on Infrared, Millimeter, and Terahertz Waves (IRMMW-THz), Paris, France, 01–06 September 2019 (2019). <https://doi.org/10.1109/IRMMW-THz.2019.8874242>
- [45] Thomas, L., Hannotte, T., Santos, C.N., Walter, B., Lavancier, M., Eliet, S., Faucher, M., Lampin, J.-F., Peretti, R.: Imaging of thz photonic modes by scattering scanning near-field optical microscopy. *ACS Applied Materials Interfaces* **14**, 32608–32617 (2022) <https://doi.org/10.1021/acsami.2c01871>
- [46] Feres, F.H., Barcelos, I.D., Mayer, R.A., Santos, T.M., Freitas, R.O., Raschke, M.B., Bahamon, D.A., Maia, F.C.B.: Dipole modelling for a robust description of subdiffractive polariton waves. *Nanoscale* **11**(44), 21218–21226 (2019) <https://doi.org/10.1039/C9NR00000A>

[//doi.org/10.1039/C9NR07387F](https://doi.org/10.1039/C9NR07387F)

- [47] Sun, Z., Andersen, T.I., Fei, Z., Liu, M., Shao, Y., Watanabe, K., Taniguchi, T., Thiemens, M., Keilmann, F., Jarillo-herrero, P., Fogler, M.M., Basov, D.N.: Efficiency of Launching Highly Confined Polaritons by Infrared Light Incident on a Hyperbolic Material (2017) <https://doi.org/10.1021/acs.nanolett.7b01587>
- [48] Yoxall, E., Schnell, M., Nikitin, A.Y., Txoperena, O., Woessner, A., Lundeberg, M.B., Casanova, F., Hueso, L.E., Koppens, F.H.L.L., Hillenbrand, R.: Direct observation of ultraslow hyperbolic polariton propagation with negative phase velocity. *Nature Photonics* **9**(10), 674–678 (2015) <https://doi.org/10.1038/nphoton.2015.166>
- [49] Duan, J., Chen, R., Li, J., Jin, K., Sun, Z., Chen, J.: Launching Phonon Polaritons by Natural Boron Nitride Wrinkles with Modifiable Dispersion by Dielectric Environments. *Advanced Materials* **1702494**, 1–8 (2017) <https://doi.org/10.1002/adma.201702494>
- [50] Maia, F.C.B., O'Callahan, B.T., Cadore, A.R., Barcelos, I.D., Campos, L.C., Watanabe, K., Taniguchi, T., Deneke, C., Belyanin, A., Raschke, M.B., Freitas, R.O.: Anisotropic Flow Control and Gate Modulation of Hybrid Phonon-Polaritons. *Nano Letters* **19**(2), 708–715 (2019) <https://doi.org/10.1021/acs.nanolett.8b03732>
- [51] Woessner, A., Lundeberg, M.B., Gao, Y., Principi, A., Alonso-González, P., Carrega, M., Watanabe, K., Taniguchi, T., Vignale, G., Polini, M., Hone, J., Hillenbrand, R., Koppens, F.H.L.: Highly confined low-loss plasmons in graphene–boron nitride heterostructures. *Nature Materials* **14**(4), 421–425 (2015) <https://doi.org/10.1038/nmat4169>
- [52] Giles, A.J., Dai, S., Vurgaftman, I., Hoffman, T., Liu, S., Lindsay, L., Ellis, C.T., Assefa, N., Chatzakis, I., Reinecke, T.L., Tischler, J.G., Fogler, M.M., Edgar, J.H., Basov, D.N., Caldwell, J.D.: Ultralow-loss polaritons in isotopically pure boron nitride. *Nature Materials* **17**(2), 134–139 (2018) <https://doi.org/10.1038/NMAT5047>
- [53] Zhang, J., Huang, Y., Tan, Z., Li, T., Zhang, Y., Jia, K., Lin, L., Sun, L., Chen, X., Li, Z., Tan, C., Zhang, J., Zheng, L., Wu, Y., Deng, B., Chen, Z., Liu, Z., Peng, H.: Low-temperature heteroepitaxy of 2d pbi2/graphene for large-area flexible photodetectors. *Advanced Materials* **30**(36), 1803194 (2018) <https://doi.org/10.1002/adma.201803194> <https://advanced.onlinelibrary.wiley.com/doi/pdf/10.1002/adma.201803194>
- [54] Zheng, W., Zheng, B., Yan, C., Liu, Y., Sun, X., Qi, Z., Yang, T., Jiang, Y., Huang, W., Fan, P., Jiang, F., Ji, W., Wang, X., Pan, A.: Direct vapor growth of 2d vertical heterostructures with tunable band alignments and interfacial charge transfer behaviors. *Advanced*

Science **6**(7), 1802204 (2019) <https://doi.org/10.1002/advs.201802204>
<https://advanced.onlinelibrary.wiley.com/doi/pdf/10.1002/advs.201802204>

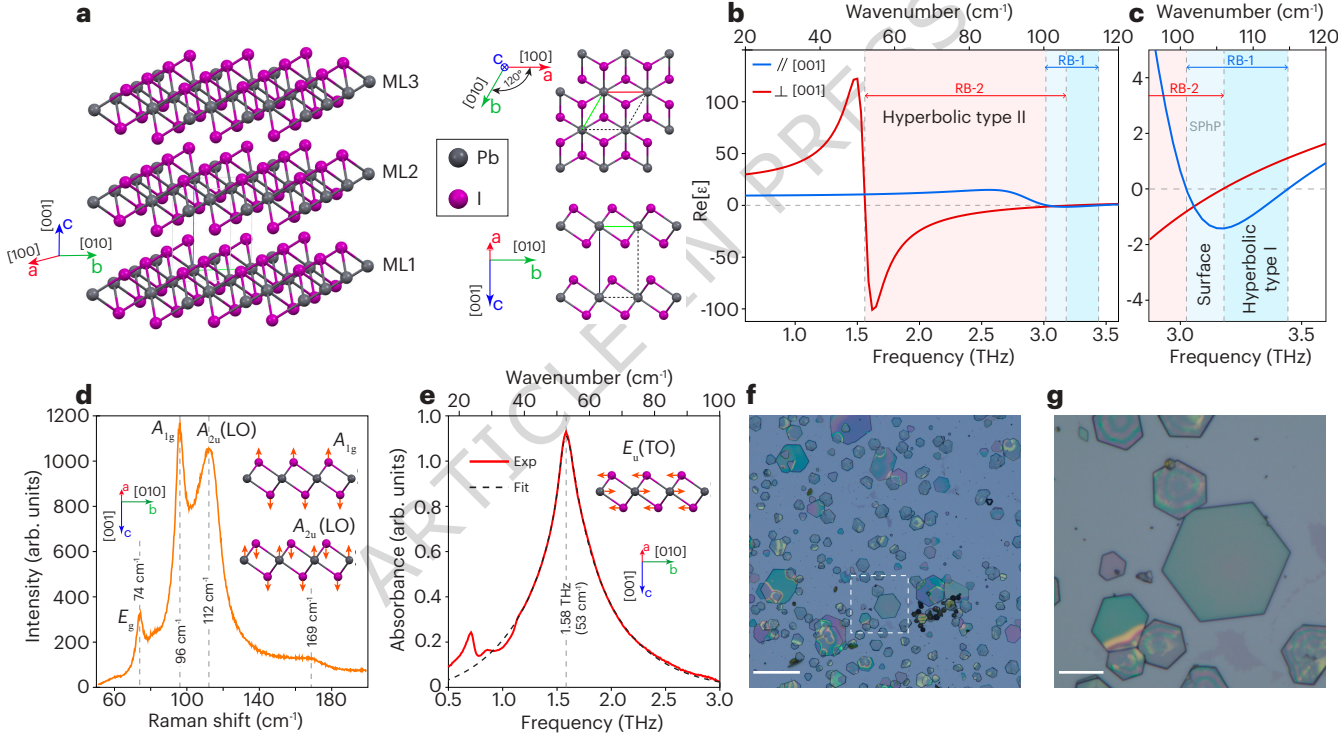
- [55] Poudyal, S., Deka, M., Adhikary, P., D, R., Barman, P.K., Yadav, R., Biswal, B., Rajarapu, R., Mukherjee, S., Nanda, B.R.K., Singh, A., Misra, A.: Room Temperature, Twist Angle Independent, Momentum Direct Interlayer Excitons in van der Waals Heterostructures with Wide Spectral Tunability. *Nano Letters* **24**(31), 9575–9582 (2024) <https://doi.org/10.1021/acs.nanolett.4c02180>
- [56] Lu, G., Pan, Z., Gubbin, C.R., Kowalski, R.A., De Liberato, S., Li, D., Caldwell, J.D.: Launching and Manipulation of Higher-Order In-Plane Hyperbolic Phonon Polaritons in Low-Dimensional Heterostructures. *Advanced Materials* **35**(22), 2300301 (2023) <https://doi.org/10.1002/adma.202300301>
- [57] Chen, N., Teng, H., Hu, H., García de Abajo, F.J., Hillenbrand, R., Dai, Q.: Boundary-induced excitation of higher-order hyperbolic phonon polaritons. *Nature Photonics* **19**(11), 1225–1232 (2025) <https://doi.org/10.1038/s41566-025-01755-5>
- [58] Slavich, A., Ermolaev, G., Pak, N., Grudinin, D., Kravtsov, K., Tatmyshevskiy, M., Semkin, V., Syuy, A., Mazitov, A., Minnekhanov, A., Kazantsev, I., Dyubo, D., Eghbali, A., Yakubovsky, D., Kashchenko, M., Podobrii, M., Titova, E., Melentev, A., Zhukova, E., Tselikov, G., Kruglov, I., Svintsov, D., Novikov, S., Vyshnevyy, A., Arsenin, A., Novoselov, K.S., Volkov, V.: Multifunctional van der Waals PdSe₂ for light detection, guiding and modulation. *Nature Communications* **16**(1), 9201 (2025) <https://doi.org/10.1038/s41467-025-64247-8>

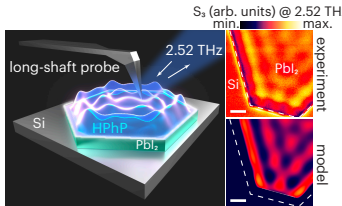
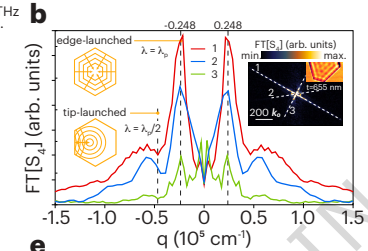
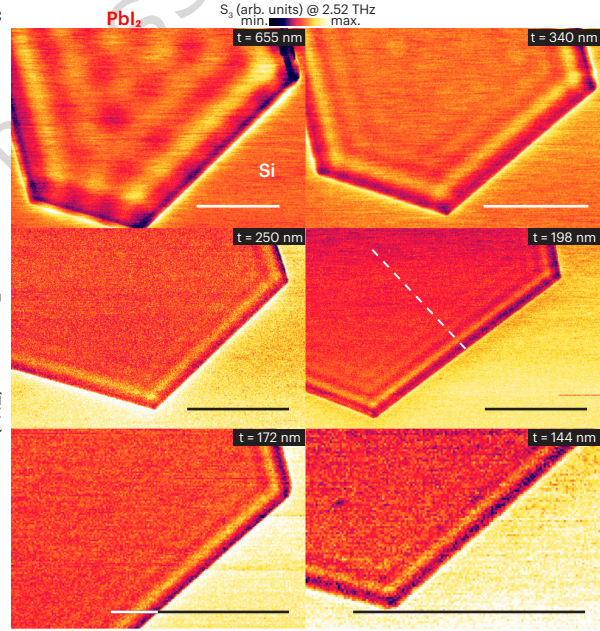
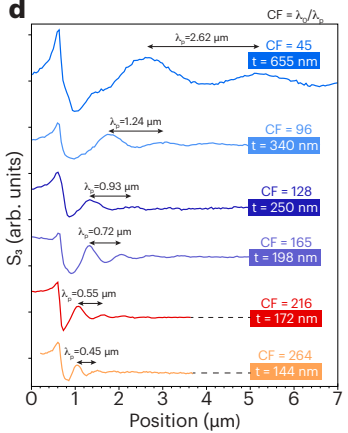
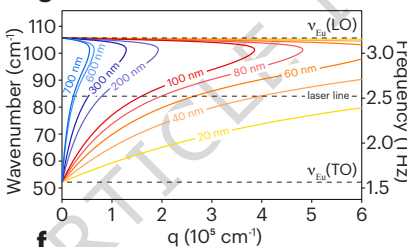
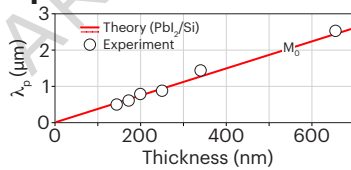
Acknowledgements. The authors thank O. Lancry (HORIBA) for the acquisition of the Raman spectra, H. Hassani (attocube systems GmbH) for the assistance on the s-SNOM TDS experiments, T. Reck, J. Hesler (VDI Inc.) for their precious help concerning the Schottky diode detection and C. Boyaval for performing SEM imaging. This work benefited from the financial support of the Agence Nationale de Recherche projects QUICKTERA (ANR-22-CE09-0018, J.-F.L. and S.E.), HYPSTER (ANR-20-CE42-0016, M.F., B.W., R.P., T.H., C.N.S., J.-F.L. and S.E.), NANOFUTUR (ANR 21-ESRE-0012, M.F.) and TRAPIST (ANR-21-CE24-0011, M.W., C.N.S. and J.-F.L.). T.H. and R.P. thanks the ERC-2022-COG grant TUSCany #101089040 for the support. R.O.F. and J.-F.L. acknowledge FAPESP (processes 2022/14245-4 and 2024/09159-7). F.H.F and R.O.F. acknowledge FAPESP post-doc project process 2023/09839-5. R.O.F. acknowledges FAPESP Young Investigator process 2019/14019-7 and CNPq grants 309946/2021-2, 300197/2025-0. We also thank CPER P4S and CPER Wavetech@hdf and the RENATECH network.

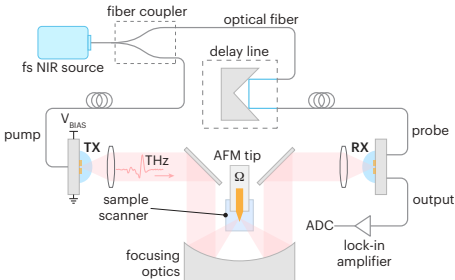
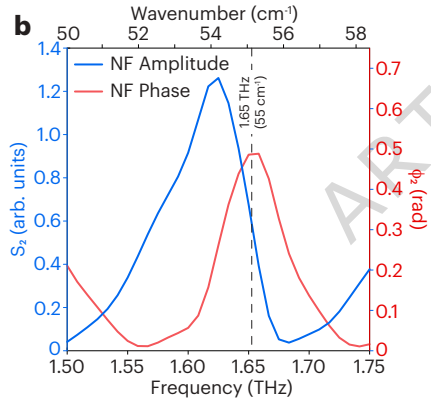
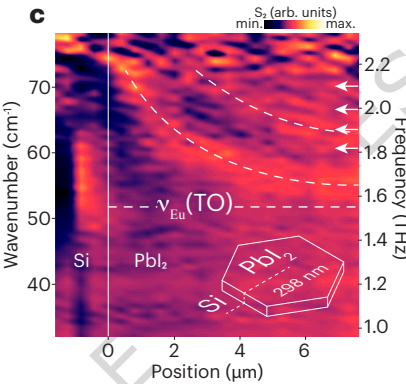
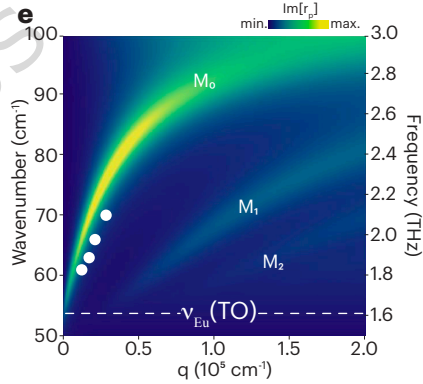
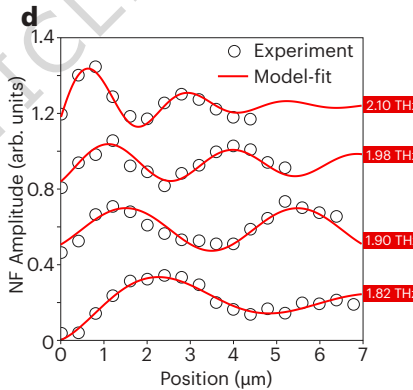
Author contribution. J.-F.L. proposed and synthesized the material. C.N.S., R.O.F., and J.-F.L. conducted the s-SNOM experiments at IEMN. R.O.F., J.-F.L., and A.C. carried out the s-SNOM TDS measurements at Attocube. C.N.S., M.V.,

and F.H.F. provided the dispersion curves. F.H.F. performed the real-space polariton waves simulations. C.N.S. and F.H.F. extracted key polariton parameters from the experiments. T.H., S.E. and R.P. conducted the far-field TDS measurements and analysis. B.W. and M.F. developed the long s-SNOM tips. C.N.S., R.O.F., and J.-F.L. co-wrote the manuscript. R.O.F. and J.-F.L. supervised the project. All authors contributed to the discussion of results and the review of the manuscript.

Competing interests. B.W. and M.F. are cofounder of Vmicro SAS, a company producing AFM and s-SNOM probes. Special probes designed and fabricated by the company were used in this study. This does not compromise the objectivity, integrity, and value of this publication. The remaining authors declare no competing interests.



a**b****c****d****e****f**

a**b****c****e****d****f**